Junyan Wang
Xin Fan
Junyu Cai ✉

https://doi.org/10.21278/TOF.503079325
ISSN 1333-1124
eISSN 1849-1391

MODELLING AND NOVEL NEURAL NETWORK PREDICTIVE CONTROL OF A FIXED DISPLACEMENT MOTOR SYSTEM CONTROLLED BY AN ELECTROHYDRAULIC PROPORTIONAL VARIABLE DISPLACEMENT PUMP

Summary

This paper proposes a neural network predictive control (NNPC) method to address the challenge of controlling the output speed in a fixed displacement motor (FDM) system controlled by an electrohydraulic proportional variable displacement pump (EHP-VDP). The dynamic response of the system is divided into four segments, and mathematical models are derived for each segment. The system is modelled using over 400 input-output data pairs, with 75% of the data used for training and the remaining 25% for validation. The Levenberg-Marquardt algorithm (LMA) is employed to optimise the neural network, achieving optimal validation performance with a mean square error of 0.0029637 after 258 epochs. This real-time optimisation enables the output speed of the system to accurately track the reference speeds. Simulink simulations are conducted over a 25-second duration covering five reference speed intervals, demonstrating reliable tracking performance. The NNPC method shows competitive performance compared with backpropagation-neural network-proportional integral derivative (BP-NN-PID) and proportional integrative derivative (PID) controllers, achieving the root mean square error (RMSE), the mean absolute error (MAE), and the integral squared error (ISE) values of 6.72, 1.00, and 572.89, respectively. These results indicate that the NNPC offers advantages in fast-response scenarios while maintaining acceptable tracking accuracy.

Key words: *electrohydraulic proportional control; pump-controlled motor system; neural network predictive control; backtracking search method*

1. Introduction

The hydromechanical continuously variable transmission (HMCVT) combines a hydraulic static transmission (HST) with mechanical components in parallel, enabling power transmission and stepless speed regulation [1-2]. The HST typically incorporates an electrohydraulic proportional variable displacement pump paired with a fixed displacement motor, where the pump-motor interaction and control mechanisms critically affect speed stability [3-4]. However, due to strong nonlinearities, time-varying characteristics, and load-dependent dynamics, pump-controlled motor systems exhibit complex transient behaviours, necessitating advanced and robust control strategies [5-6].

Recent studies have explored various control methods to cope with these nonlinearities. Zeng et al. [7] proposed a three-step variable pump displacement control method that significantly improved performance compared with traditional PID controller-based strategies. Liu et al. [8] developed a nonlinear proportional-integral control method for variable pump mechanism regulation, showing notable control effects. Cao et al. [9] developed a speed control strategy combining double feedforward with a fuzzy PID controller, effectively mitigating the impacts of the step speed input on system stability. Lu et al. [10] introduced a fuzzy PID control algorithm based on improved particle swarm optimisation, precisely tracking the motor speed. Although these studies demonstrate an enhanced dynamic response, they remain largely rooted in conventional PID frameworks, leading to limited progress in intelligent or data-driven control applications [11-14].

In contrast, recent literature has begun exploring intelligent black-box modelling and learning-based control for hydraulic transmission systems. For example, a study on the HST stroke control introduced an artificial neural network (ANN) controller that imitates multiple model predictive control, showing superior robustness to stochastic disturbances, strong nonlinear tracking capability, and improved computational efficiency in processor-in-the-loop simulations [15]. Similarly, experimental research on GEROLER hydraulic motors demonstrated that neural network-based black-box models - particularly dynamic nonlinear autoregressive networks with exogenous inputs (NARX structures) - can effectively capture nonlinear motor dynamics under uneven load torque, outperforming traditional modelling approaches in prediction accuracy and adaptability [16]. These findings highlight the growing feasibility and advantages of applying machine learning-based modelling and prediction methods in nonlinear hydraulic systems.

Motivated by these developments, this study introduces a neural network predictive control (NNPC) approach [17-18] to achieve fast and high-precision speed regulation in a fixed displacement motor (FDM) system controlled by an electrohydraulic proportional variable displacement pump (EHP-VDP). The NNPC integrates the neural network system identification with predictive control strategies to enhance control accuracy and dynamic adaptability. Simulation experiments on the Simulink platform were conducted to evaluate the NNP controller's performance in regulating the system output speed, focusing on its robustness and adaptability. Using RMSE, MAE, and ISE as key performance metrics, the NNPC was compared with conventional control schemes, showing competitive performance and reliable adaptability in addressing control challenges typical of nonlinear and complex hydraulic systems.

2. Model of the FDM system controlled by an EHP-VDP

This paper studies an FDM system controlled by an EHP-VDP that employs electrohydraulic proportional control technology. It plays a crucial role in providing stepless speed regulation and power transmission in HMCVT, with its structural principle illustrated in Fig. 1.

In an FDM system controlled by an EHP-VDP, the transmission control unit (TCU) generates a command voltage that actuates the proportional solenoid. The solenoid regulates the position of the electrohydraulic proportional valve spool, thereby adjusting both the flow rate and the flow direction of the hydraulic fluid entering the control cylinder. The resulting pressure differential across the hydraulic cylinder chambers drives the piston rod, which is mechanically linked to the swashplate of a variable displacement pump. As the piston rod moves, it changes the swashplate angle, thus altering the geometric displacement of the axial piston pump. Since the pump and the motor form a closed-type hydrostatic transmission, any change in the pump displacement directly modifies the hydraulic flow delivered to the fixed displacement motor. Consequently, the motor speed adjusts proportionally to the commanded displacement, enabling continuous and precise control of the system output speed. This sequence of electromechanical-hydraulic interactions establishes a closed-loop control mechanism that enables real-time, stepless speed regulation of the motor.

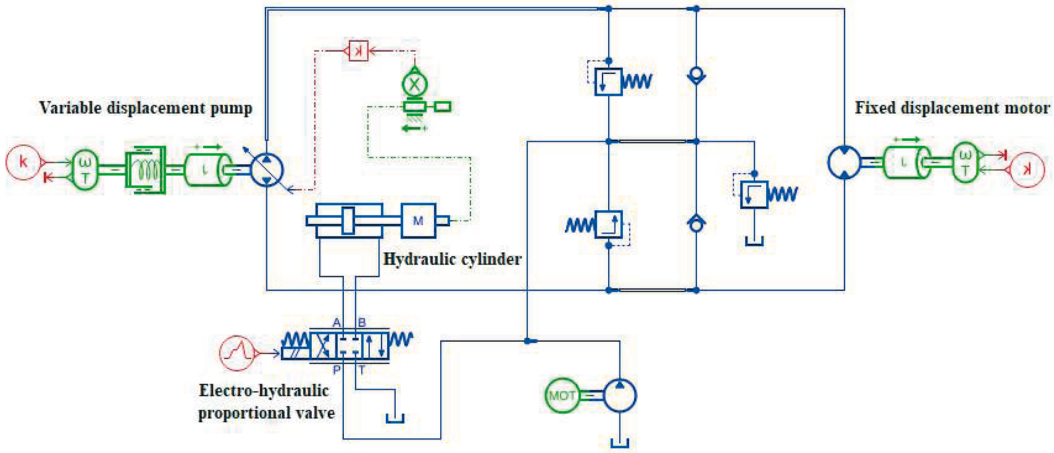

Fig. 1 Structure of an FDM system controlled by an EHP-VDP

The dynamic response of the complete system can be divided into four stages: (1) the dynamic response of the valve spool displacement of the electrohydraulic proportional control valve after receiving a given voltage signal; (2) the dynamic response of the hydraulic cylinder piston displacement to the valve spool displacement of the electrohydraulic proportional control valve; (3) the dynamic response of the variable displacement pump swashplate angle to the hydraulic cylinder piston displacement; (4) the dynamic response of the fixed displacement motor's rotational speed to the variable displacement pump swashplate angle. The complete dynamic response process is shown in Fig. 2.

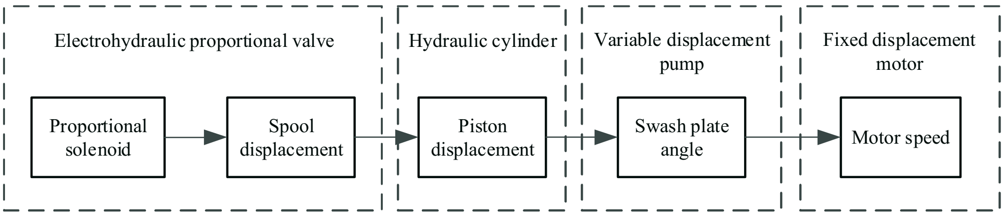

Fig. 2 Dynamic response process of an FDM system controlled by an EHP-VDP

2.1 Mathematical model of the electrohydraulic proportional control valve

The valve spool of the electrohydraulic proportional control valve is directly driven by a proportional solenoid. The push rod of the proportional solenoid pushes the spool to move against the forces of steady hydraulic pressure, inertia, and spring force. Since the displacement of the control valve spool is equal to the displacement of the armature of the proportional solenoid, the transfer function $W_1(s)$, with the given voltage $U_g(s)$ as the input and the spool displacement $X_v(s)$ as the output, is given by:

$$W_1(s)=\frac{X_v(s)}{U_g(s)}=\frac{K_eK_i/K_{et}L_c\omega_e}{\frac{s^3}{\omega_e\omega_v^2}+s^2(\frac{1}{\omega_v^2}+\frac{2\delta_v}{\omega_e\omega_v})+s(\frac{1}{\omega_e}+\frac{2\delta_v}{\omega_v}+\frac{K_iK_b}{K_{et}L_c\omega_e})+1+\frac{K_eK_iK_{xef}}{K_{et}L_c\omega_e}} \tag{1}$$

$$\omega_e=\frac{R_c+r_p+K_{fi}K_e}{L_c} \tag{2}$$

$$\omega_v = \sqrt{\frac{K_{et}}{m_e + m_v}} \tag{3}$$

$$\delta_v = \frac{B_e + B_v}{2\sqrt{K_{et}(m_e + m_v)}} \tag{4}$$

$$K_{et} = K_v + K_{fv} \tag{5}$$

2.2 Mathematical model of the valve-controlled hydraulic cylinder

The variable mechanism of the electrohydraulic proportional variable displacement pump includes a four-way slide valve and symmetrical hydraulic cylinders. The displacement of the four-way slide valve spool changes the flow direction of the hydraulic piping, generating hydraulic pressure to move the piston of the hydraulic cylinder. Therefore, the transfer function of this stage $W_2(s)$, with the spool displacement $X_v(s)$ as the input and the piston displacement $X_p(s)$ as the output, is given by:

$$W_2(s) = \frac{X_p(s)}{X_v(s)} = \frac{K_q / A_p}{s(\frac{s^2}{\omega_h^2} + \frac{2\delta_h}{\omega_h} s + 1)} \tag{6}$$

$$\omega_h = 2A_p \sqrt{\frac{\beta_e}{m_t V_t}} \tag{7}$$

$$\delta_h = \frac{C_{tc}}{A_p} \sqrt{\frac{\beta_e m_t}{V_t}} \tag{8}$$

If a displacement sensor K_f is used to provide feedback of the displacement of the hydraulic cylinder, forming a small closed loop for displacement, it can eliminate the preceding integration section [19]. In summary, the first two dynamic response stages reflect the control process of the variable mechanism in the FDM system controlled by an EHP-VDP, with the given voltage $U_g(s)$ as input and the piston displacement $X_p(s)$ as output, and the dynamic characteristics of the closed-loop transfer function $G_1(s)$ are given by:

$$G_1(s) = \frac{X_p(s)}{U_g(s)} = \frac{W_1(s)W_2(s)}{1 + W_1(s)W_2(s)K_f} \tag{9}$$

2.3 Mathematical model of the axial piston pump

In this system, the piston rod of the hydraulic cylinder is mechanically linked to the swashplate mechanism of the variable displacement pump. The pump used in this study is an axial piston pump, whose displacement is regulated by the swashplate angle γ(s), which determines the stroke of its pistons.

It should be noted that the axial piston pump contains its own internal pump cylinders, arranged around the drive shaft, which operate independently of the main hydraulic cylinder controlled by the proportional valve. Thus, the pump displacement is governed solely by the swashplate angle and the rotation of the cylinder block.

Based on this operating principle, the transfer function of this subsystem $W_3(s)$ can be expressed as:

$$W_3(s) = \frac{\gamma(s)}{X_p(s)} = \frac{1}{D} \tag{10}$$

2.4 Mathematical model of the FDM system controlled by a VDP

The FDM system controlled by a VDP is the most commonly used form of pump-controlled hydraulic motor system. The variable displacement pump rotates at a constant speed ω_p, controlling the speed and rotation direction of the hydraulic motor by adjusting the pump displacement. After appropriately simplifying the system, the transfer function of this stage $W_4(s)$ can be expressed as:

$$W_4(s) = \frac{\omega_m(s)}{\gamma(s)} = \frac{K_p \omega_p / D_m}{\dfrac{s^2}{\omega_{pm}^2} + \dfrac{2\delta_{pm}}{\omega_{pm}} s + 1} \tag{11}$$

$$\omega_{pm} = D_m \sqrt{\frac{\beta_e}{J_m V_0}} \tag{12}$$

$$\delta_{pm} = \frac{C_t J_m}{2D_m} \sqrt{\frac{\beta_e}{J_m V_0}} \tag{13}$$

2.5 Transfer function of the FDM system controlled by an EHP-VDP

In summary, based on the transfer functions of the four dynamic response stages, we can obtain the transfer function $G(s)$ of the FDM system controlled by an EHP-VDP. The block diagram of the system transfer function is shown in Fig. 3.

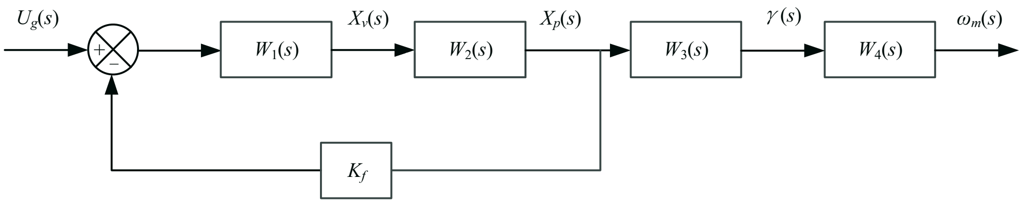

Fig. 3 System transfer function block diagram

$G(s)$ outputs the rotational speed $\omega_m(s)$ of the fixed displacement motor, with the given voltage $U_g(s)$ to the proportional solenoid as its input, and its expression is:

$$G(s) = \frac{\omega_m(s)}{U_g(s)} = \frac{W_1(s)W_2(s)}{1 + W_1(s)W_2(s)K_f} \cdot W_3(s) \cdot W_4(s) \tag{14}$$

3. Design of an NNP controller

3.1 System identification

The first task of the NNP control is to use the neural network model to identify the plant. It requires a selection of a specific learning algorithm and uses the error between the output y_p of the plant and the output y_m of the neural network model to complete the neural network modelling. This process is known as system identification, as shown in Fig. 4.

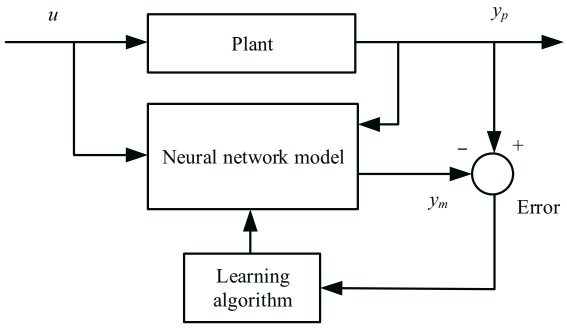

Fig. 4 System identification process

By system identification, a neural network model is obtained. Its input is the model input $u(t)$ at the current time t and the output $y_p(t)$ of the plant, and its output is the predicted output value $y_m(t+1)$ of the plant at the next moment $(t+1)$. The specific structure of the neural network identification model is shown in Fig. 5.

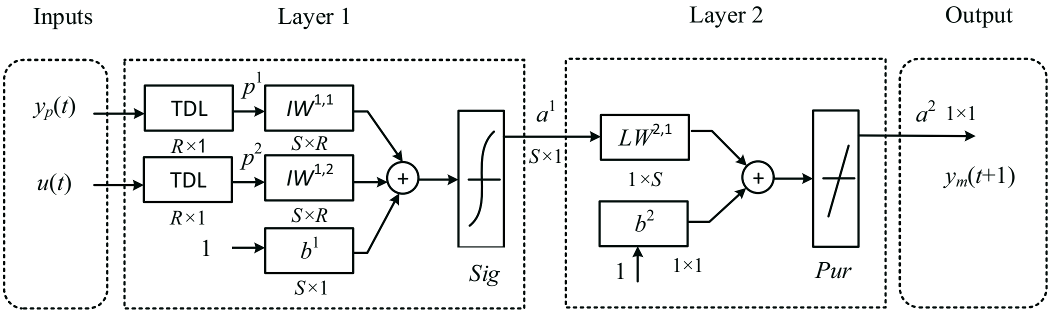

Fig. 5 Structure of the neural network model

This paper uses the Levenberg-Marquardt algorithm (LMA) as the learning algorithm of the neural network model [20]. Using data randomly collected from the operation of the plant, the offline training of the neural network model is completed in the batch learning mode. Like quasi-Newton methods, the LMA uses the second-order curvature information of the error surface but does not require the calculation of the Hessian matrix. When the performance index function $V(x_t)$ is set in the form of a sum of squares, the Hessian matrix $H(x_t)$ can be approximated as:

$$H(x_t) = A(x_t)^T A(x_t) \tag{15}$$

$$V(x_t) = \sum_{i=1}^{N} e_i^2(x_t) = \sum_{i=1}^{N} (y_{pi}(x_t) - y_{mi}(x_t))^2 \quad , \tag{16}$$

where x_t represents the vector of all parameters to be updated at time t; N is the number of output variables of the neural network identification model; $A(x_t)$ is the Jacobian matrix, which includes the first-order derivatives of the neural network error with respect to all parameters to be updated, with the total number of these parameters being N; and $e(x_t)$ is the neural network error vector.

At this point, the gradient $g(x_t)$ is calculated according to Eq. (17) as follows:

$$g(x_t) = A(x_t)^T e(x_t) \tag{17}$$

The Jacobian matrix $A(x_t)$ can be calculated using standard backpropagation techniques [21-22] as follows:

$$A(x_t) = \begin{bmatrix} \dfrac{\partial e_1(x_t)}{\partial x_1} & \cdots & \dfrac{\partial e_1(x_t)}{\partial x_n} \\ \vdots & \ddots & \vdots \\ \dfrac{\partial e_N(x_t)}{\partial x_1} & \cdots & \dfrac{\partial e_N(x_t)}{\partial x_n} \end{bmatrix} \tag{18}$$

The LMA utilises an approximation of the Hessian matrix to achieve an iteration process similar to Newton's method:

$$x_{t+1} = x_t - [A(x_t)^T A(x_t) + \mu I]^{-1} A(x_t)^T e(x_t), \tag{19}$$

where x_{t+1} is the vector of all parameters after one iteration update at time $(t+1)$ and μ is the damping parameter. When the value of μ is zero, Eq. (19) represents Newton's method using the approximate Hessian matrix; when the value of μ is large, Eq. (19) becomes the gradient descent method with a smaller step size. Newton's method is faster and more accurate when close to the minimum error, and therefore the optimisation goal is to switch to Newton's method as quickly as possible. After each successful step (i.e., whenever the performance index function $V(x_t)$ decreases), μ is reduced, ensuring that the performance index function always decreases with each iteration of the algorithm.

3.2 Predictive control

The prediction of the neural network model employs a rolling time-domain method [23-24], obtaining the predicted values of the plant within a specified time domain. Through a numerical optimisation program, the optimal control signal is sought to minimise the objective function $J(t)$ as follows:

$$J(t) = \sum_{j=N_1}^{N_2} [y_r(t+j) - y_m(t+j)]^2 + \rho \sum_{j=1}^{N_u} [u'(t+j-1) - u'(t+j-2)]^2, \tag{20}$$

where N_1 and N_2 define the range of the error-prediction time domain, with N_1 typically set to 1; N_u is the control-increment time-domain range; y_r is the desired response output value of the controlled object system; y_m is the response output value of the neural network identification model; and u' is the transitional control signal.

The coefficient ρ denotes the weight assigned to the sum of squares of control increments in the performance index function, thereby balancing the trade-off between the output error and the control variation. A smaller ρ value emphasises minimising output errors but may cause excessive control signal variations, which may affect system stability. In contrast, a larger ρ value penalises control increments more heavily, resulting in smoother control signals but potentially slower system responses and reduced tracking performance.

The prediction process of the neural network model is illustrated in Fig. 6, where the NNP controller consists of a neural network identification model and a numerical optimisation program. By continuously optimising the performance index function $J(t)$ to achieve its minimisation, the obtained optimal control quantities u' and u are passed to the neural network identification model and the plant, respectively, thereby achieving optimal control of the controlled object system.

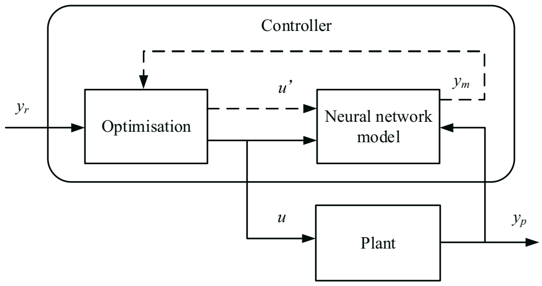

Fig. 6 Prediction process of the neural network model

Along the given descent direction p_k, the optimisation is carried out on the performance index function $J(t)$ to obtain the iterative formula for the control variable u as follows:

$$u(t+1)=u(t)+\lambda_k p_k \tag{21}$$

$$p_k=-\frac{\partial J(t)}{\partial u(t)} \tag{22}$$

The numerical optimisation program uses a backtracking search method to find its path to minimisation, which is a type of line search algorithm [25]. Initially, set λ_k=1; if $u(t)+p_k$ does not meet the requirements, then perform backtracking search (i.e., decrease λ_k) until finding a $u(t)+\lambda_k p_k$ that satisfies them. In the first step of the calculation, the performance index function value $J(t)$ at the current point $u(t)$, the performance index function value $J(t)$ at $u(t)+p_k$, and the derivative of the performance index function value $J(t)$ at $u(t)$ are used to obtain a quadratic approximation equation of the performance index function along the search direction. The minimum value of this quadratic approximation is taken as a provisional optimal point, and the performance index function value $J(t)$ at this point is calculated. If there is no sufficiently significant reduction, a cubic approximation equation is calculated, and the minimum value of the cubic approximation becomes the new provisional optimal point, until a significant reduction in the performance index function value $J(t)$ is achieved.

4. Simulation experiments and analysis of the results

In this study, simulation-generated data are used to develop and preliminarily validate the proposed control strategy. Synthetic data can offer a controlled variation of inputs, enable the creation of diverse and repeatable scenarios, and provide access to accurate ground truth data. These features are expected to make simulation a practical approach for early-stage evaluation before the subsequent hardware testing.

4.1 Simulation experiment procedure

Based on the transfer function Eq. (14), we can derive a differential equation for the FDM system controlled by an EHP-VDP as follows:

$$a_1 y^{(8)}+a_2 y^{(7)}+a_3 y^{(6)}+a_4 y^{(5)}+a_5 y^{(4)}+a_6\dddot{y}+a_7\ddot{y}+a_8\dot{y}+a_9 y=bu\,, \tag{23}$$

where a_1, a_2, a_3, a_4, a_5, a_6, a_7, a_8, a_9, and b are the coefficients of the differential equation in Eq. (23).

The simulation experiments in this paper were conducted on the Simulink platform within MATLAB. The input value $u(t)$ of the plant was set to random numbers in the range [0,24], which were substituted into the system differential Eq. (23), resulting in 400 sets of sample data. Among these, 300 sets were used as the training set and 100 sets as the validation set. The input and the output data of the resulting neural network identification model are shown in Fig. 7.

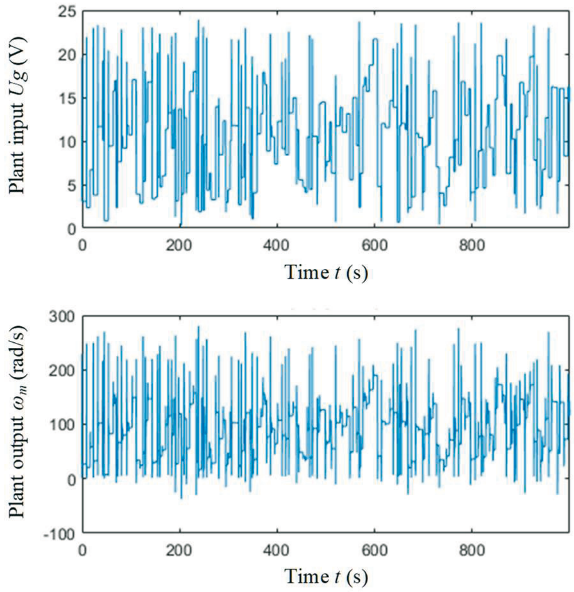

Fig. 7 Input and output data of the plant

The neural network identification model is configured with the following parameters: the number of neurons in the hidden layer (S) is set to 7, and the input and the output delay parameters (R) are set to two sampling periods. Consequently, the input vector p_t of the neural network identification model is defined as follows:

$$p_t = [y_p(t-1), y_p(t-2), u(t-1), u(t-2)]^T \tag{24}$$

The offline training results of the neural network identification model are shown in Fig. 8, where Fig. 8a presents the training data results and Fig. 8b presents the validation data results. The system identification results indicate that, under the same input data, the plant and the neural network identification model have nearly identical output results. The system output error is controlled within ±1 rad/s, demonstrating that the neural network identification model can effectively substitute for the plant in subsequent predictive control processes.

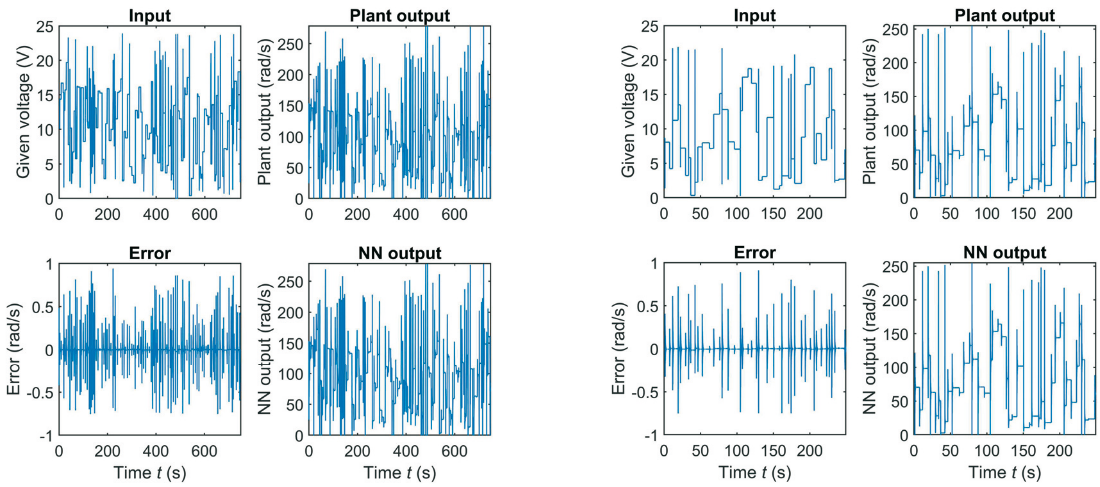

(a) Training data

(b) Validation data

Fig. 8 Off-line training results of the neural network identification model

The neural network model learning parameters were set as follows: The maximum training epochs for the neural network model were set to 300, with the training algorithm being the LMA. The training results of the neural network model indicate that it underwent a total of 264 training iterations, achieving the best validation performance at the 258th iteration, where the mean square error was 0.0029637, below the preset threshold of 0.01; thus, the neural network identification model achieved high predictive accuracy after training. The iterative process of the neural network identification model is shown in Fig. 9.

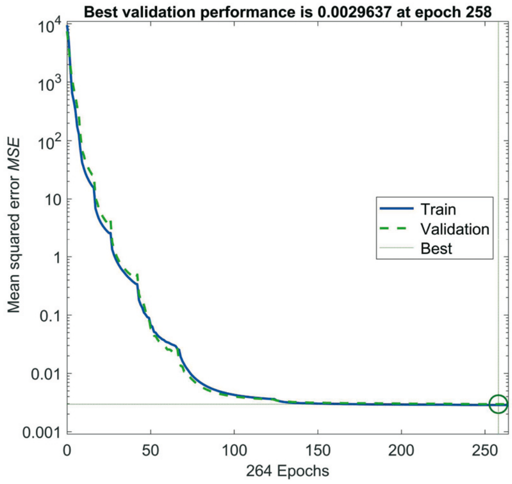

Fig. 9 Iterative process of the neural network identification model

After completing the system identification, the neural network model can participate in the predictive control process of the FDM system controlled by an EHP-VDP.

The parameter values of the NNPC are not predefined. Therefore, similarly to the system identification phase, we determine all variables in the predictive control through multiple simulation trials, selecting optimal values based on the observed system performance indicators. Finally, the simulation values of the model predictive control parameters were set as follows: the lower limit of the error prediction time domain was $\boldsymbol{N_1}$=1; the upper limit of the error prediction time domain was $\boldsymbol{N_2}$=10; the upper limit of the control increment time domain was $\boldsymbol{N_u}$=2; the control proportion factor was $\boldsymbol{\rho}$=0.05; the sampling time was 0.1 s; the minimisation path was set to "csrchbac" (i.e., the backtracking search method); and the number of iterations of the optimisation algorithm executed within each sampling time was 2.

The numerical simulation time was set to 25 s, divided into five stages: [0,5) s, [5,10) s, [10,15) s, [15,20) s, and [20,25] s. The desired output values of the plant (i.e., desired motor speeds) were randomly generated by the algorithm program, which were 37, 134, 164, 96, and 149 rad/s, respectively. The simulation parameters of the FDM system controlled by an EHP-VDP are shown in Table 1. To improve the realism of the simulation, the key parameters in Table 1 were mainly taken from manufacturer manuals and available experimental data. Although the data were still generated computationally, this parameter selection helps the model approximate the actual electrohydraulic system as closely as feasible at this stage.

Table 1 Simulation parameters of the FDM system controlled by an EHP-VDP

Symbols	Value	Unit	Symbols	Value	Unit	Symbols	Value	Unit
K_e	2.4	-	K_i	16.3	N/A	K_v	7750	N/m
K_{fv}	6875	N/m	R_c	7	Ω	r_p	7	Ω
L_c	0.1	H	K_{fi}	1.6	V/A	K_b	1500	V·s/m
K_{xef}	1333.33	V/m	B_e	2	N·s/m	B_v	10	N·s/m
m_e	0.06	kg	m_v	0.08	kg	K_q	0.653	m^2/s
A_p	4.12×10^{-4}	m^2	K_f	800	-	β_e	7×10^{8}	N/m^2
m_t	25	kg	V_t	5×10^{-5}	m^3	C_{tc}	1.2×10^{-11}	$m^5/N\cdot s$
D	0.1	m	K_p	2.906×10^{-4}	m^3/rad^2	ω_p	210	rad/s
D_m	8.73×10^{-6}	m^3/rad	J_m	0.015	$kg\cdot m^2$	V_0	6.9×10^{-4}	m^3
C_t	5×10^{-12}	$m^5/N\cdot s$	-	-	-	-	-	-

4.2 Analysis of the simulation results

Fig. 10 shows the output speed curve of the FDM system controlled by an EHP-VDP under the NNPC method. Fig. 11 presents the corresponding curve of changes in the input control quantity (i.e., the given voltage signal) to the plant. Table 2 provides the evaluation indicators of the system's dynamic performance under the NNPC method.

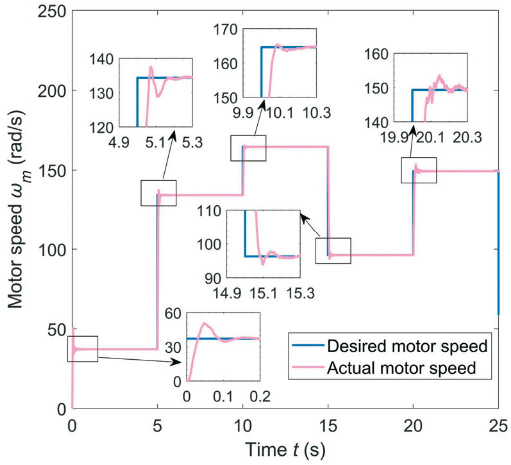

Fig. 10 Output speed curve of the plant

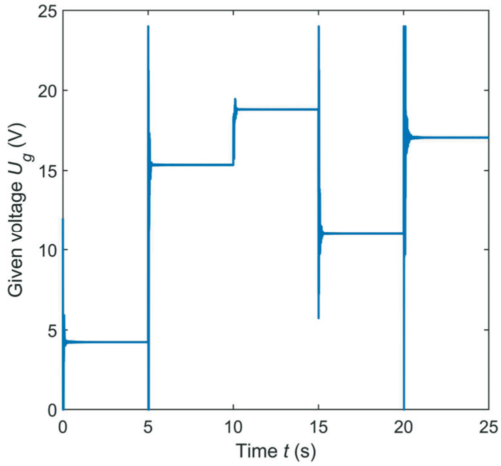

Fig. 11 Input voltage curve of the plant

Table 2 Performance indicators of the neural network predictive control method

Numerical simulation time interval (s)	Desired output value (rad/s)	Overshoot σ (%)	Settling time t_s (s) (Δ=±2%)
[0,5)	37	36.80	0.18
[5,10)	134	2.37	0.14
[10,15)	164	0.52	0.07
[15,20)	96	2.50	0.10
[20,25]	149	2.85	0.16

Note: Δ denotes the allowable error range. In the numerical simulations, a ±2% band around the steady-state reference value is adopted. The settling time t_s is defined as the moment when the system response first enters this ±2% band and subsequently remains within it without exiting again.

The analysis of the results led to the following observations:

(1) The settling times t_s in the five simulation stages are notably brief, at 0.18, 0.14, 0.07, 0.10, and 0.16 seconds. This demonstrates the system's swift dynamic response, its reactivity, and the ability of the NNP controller to rapidly converge to target outputs, ensuring prompt adjustments in control inputs.

(2) Initially, the system's response curve shows an overshoot σ of 36.8%, indicating considerable variability. However, overshoots in the later stages are reduced to 2.37%, 0.52%, 2.50%, and 2.85%, suggesting that the controller achieves more stable behaviour once the system enters smoother operating conditions.

(3) Overall, the simulation results indicate that the NNP controller is capable of achieving timely and reasonably accurate tracking performance within the tested scenarios. While certain transient overshoots remain, the controller maintains acceptable regulation quality and demonstrates its potential as a competitive option for this type of hydraulic speed-control system.

4.3 Comparison with different control methods

4.3.1 Simulation results of the BP-NN-PID and PID methods

Under the same simulation conditions as described in Section 4.1, simulation experiments were also conducted using the BP-NN-PID and PID methods. The system output curves obtained using the BP-NN-PID and PID methods are shown in Fig. 12, and the system control input curves are presented in Fig. 13. Table 3 provides the performance evaluation data for the system's dynamic characteristics under the BP-NN-PID and PID methods.

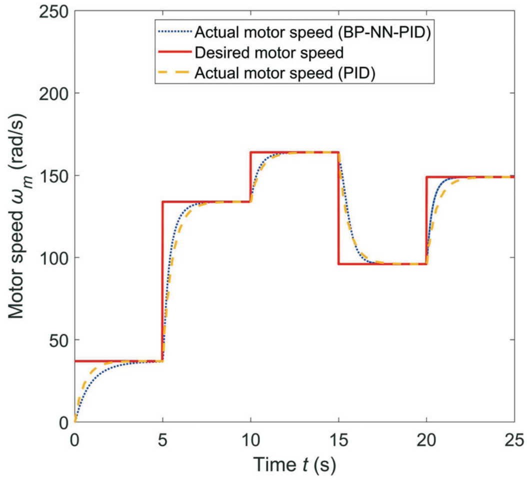

Fig. 12 System output curve with BP-NN-PID and PID methods applied

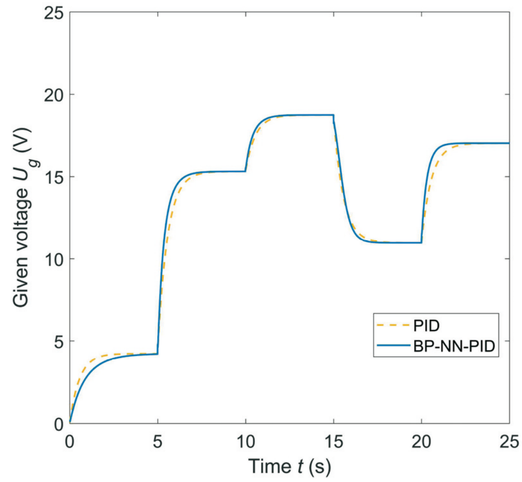

Fig. 13 System input curve with BP-NN-PID and PID methods applied

Table 3 Performance indicators of the BP-NN-PID and PID methods

Numerical simulation time interval (s)	Desired output value (rad/s)	Overshoot σ (%)		Settling time t_s (s) (Δ=±2%)	
		BP-NN-PID	PID	BP-NN-PID	PID
[0,5)	37	0	0	3.25	2.18
[5,10)	134	0	0	1.66	1.99
[10,15)	164	0	0	0.97	1.23
[15,20)	96	0	0	1.49	1.98
[20,25]	149	0	0	1.07	1.60

Note: Δ denotes the allowable error range. In the numerical simulations, a ±2% band around the steady-state reference value is adopted. The settling time t_s is defined as the moment when the system response first enters this ±2% band and subsequently remains within it without exiting again.

The analysis of Figs. 12 and 13 and Table 3 reveals:

(1) The BP-NN-PID and PID controllers effectively manage the stepless speed regulation of the FDM system controlled by an EHP-VDP. The zero overshoot (σ) observed in the system response curves across five distinct simulation stages indicates excellent system stability.

(2) Both the BP-NN-PID and the PID controllers accurately track the set points during simulation. However, the observed settling times (3.25, 1.66, 0.97, 1.49, and 1.07 seconds for the BP-NN-PID controllers, and 2.18, 1.99, 1.23, 1.98, and 1.60 seconds for the PID controllers) reveal a relatively slow dynamic response, indicating less responsive control input adjustments.

4.3.2 Comparison of the tracking performance across different control methods

Tracking performance in closed-loop hydraulic speed regulation reflects the controller’s ability to rapidly follow a reference trajectory while maintaining stability after disturbances. In practical terms, it represents a combined effect of key transient behaviours - including overshoot and settling time - as well as the steady-state accuracy achieved after the system reaches equilibrium.

To comprehensively assess the tracking performance of the proposed NNP controller, three widely used quantitative indicators - RMSE, MAE, and ISE - were selected as performance metrics [26-28]. These indicators jointly evaluate both transient and steady-state characteristics, enabling a balanced assessment of the trade-off between response rapidity and tracking smoothness.

The mathematical expressions for RMSE, MAE and ISE are given as follows:

$$RMSE = \sqrt{\frac{1}{t_1 - t_0}\int_{t_0}^{t_1}(y_p - y_r)^2 \mathrm{d}t} \tag{25}$$

$$MAE = \frac{1}{t_1 - t_0}\int_{t_0}^{t_1}\left|y_p - y_r\right| \mathrm{d}t \tag{26}$$

$$ISE = \int_{t_0}^{t_1}(y_p - y_r)^2 \mathrm{d}t\,, \tag{27}$$

where t_0 is the start time of the tracking curve, in s; t_1 is the end time of the tracking curve, in s; y_p is the output of the controlled object system, in rad/s; and y_r is the desired output of the controlled object system, in rad/s.

Table 4 Comparison of tracking performance between the three control methods

Control method/Evaluation indicators	RMSE	MAE	ISE
NNPC	6.72	1.00	572.89
BP-NN-PID	14.27	5.78	5094.10
PID	14.59	6.33	5319.58

A comparative analysis was conducted under identical simulation conditions for the NNP, BP-NN-PID, and classical PID controllers. The results are summarised in Table 4. The proposed NNP controller achieved the RMSE, MAE, and ISE values of 6.72, 1.00, and 572.89, respectively - all lower than those obtained with the BP-NN-PID controllers (RMSE: 14.27, MAE: 5.78, ISE: 5094.10) and the PID controllers (RMSE: 14.59, MAE: 6.33, ISE: 5319.58).

These results reflect the trade-off between the overshoot and the settling time among the three controllers. The BP-NN-PID and PID controllers provide a stable, overshoot-free response, while the NNP controller achieves a considerably faster transient with acceptable overshoot, which results in a smaller ISE. Accordingly, the NNP controller presents a competitive control strategy that balances rapid dynamic response with stable regulation of the output rotational speed in the FDM system controlled by an EHP-VDP.

5. Conclusions

This paper focuses on the application of the NNPC method for controlling the output rotational speed of the FDM system controlled by an EHP-VDP. The system was modelled using a neural network identification model, which converged after 264 iterations with a mean square error of 0.0029637. During the predictive control phase, gradient descent with backtracking search was used to determine the control inputs, enabling accurate tracking of reference speeds in the simulations. The evaluation of the use of RMSE, MAE, and ISE metrics indicated that the NNPC method achieves competitive performance and reliable adaptability compared with conventional BP-NN-PID and PID controllers.

It should be noted that the NNPC exhibits a small amount of overshoot compared with the aperiodic, overshoot-free responses produced by the PID controller. However, its significantly shorter settling time enables quicker convergence to the vicinity of the target speed, which contributes to the lower ISE observed in the simulations. Therefore, the primary advantage of the NNPC lies in its fast transient response rather than absolute superiority over the PID control. The method is particularly competitive in applications where rapid response is prioritised and a certain level of overshoot is acceptable. Overall, the proposed NNPC method provides an effective and competitive alternative for managing the output rotational speed of FDM systems controlled by EHP-VDPs, offering improved response rapidity while maintaining acceptable tracking performance and robustness.

Future research will first involve collecting experimental data on a physical electrohydraulic test bench, which will be used to refine the learning model and to validate the proposed control strategy under real operating conditions, including hydraulic disturbances, sensor noise, and external load variations. Secondly, the NNPC framework can be further extended to multi-variable control scenarios, where multiple actuators collaboratively regulate the hydraulic system to optimise overall control performance. Finally, the study can explore integrating reinforcement learning with NNPC to enhance the controller's adaptive capability, enabling real-time parameter adjustments in response to system state variations, thereby improving control effectiveness and response efficiency.

ACKNOWLEDGMENTS

This study was financially supported by the National Natural Science Foundation of China (No. U1564201 and No. U51675235), the Research Team Project of Zhenjiang College (GZKYTD2021007), and Zhenjiang Key Laboratory for Intelligent Collaboration, Integration and Application of Industrial Internet (No. SS2025007).

NOMENCLATURE

K_e	: Voltage amplification coefficient of the DC amplifier
K_i	: Current-to-force gain of the proportional solenoid
K_{et}	: Total stiffness
ω_e	: Cutoff frequency of the proportional solenoid coil
ω_v	: Resonance frequency of the armature and spool assembly
δ_v	: Damping ratio of the armature-spool assembly
K_v	: Stiffness of the valve spool feedback spring
K_{fv}	: Steady-state hydraulic force stiffness coefficient
R_c	: Resistance of a single coil
r_p	: Internal resistance of the amplifier
L_c	: Inductance of a single coil
K_{fi}	: Deep current negative feedback coefficient
K_b	: Back electromotive force coefficient
K_{xef}	: Displacement-to-voltage gain
B_e	: Comprehensive damping coefficient
B_v	: Viscous damping coefficient of the spool
m_e	: Mass of the armature assembly
m_v	: Mass of the valve spool assembly
K_a	: Valve's null position flow gain
A_p	: Effective working area of the hydraulic cylinder piston
ω_h	: Hydraulic natural frequency of the valve-controlled hydraulic cylinder
δ_h	: Hydraulic damping ratio of the valve-controlled hydraulic cylinder
β_e	: Effective bulk modulus
m_t	: Total mass of the piston and load
V_t	: Total effective volume of the hydraulic cylinder
C_{tc}	: Total leakage coefficient of the hydraulic cylinder
K_f	: Displacement sensor coefficient
D	: Distance between force application point of hydraulic cylinder piston and pivot point of the swashplate
K	: Displacement gradient of variable displacement pump
ω	: Rotational speed of the variable displacement pump
D	: Displacement of the hydraulic motor
ω_{pm}	: Hydraulic natural frequency of FDM system controlled by VDP
δ_{pm}	: Hydraulic damping ratio of FDM system controlled by VDP
J	: Rotational inertia of the hydraulic motor

V_0 : Total volume of high-pressure chamber and piping of variable displacement pump and hydraulic motor
C_t : Total leakage coefficient of the system
x_t : Vector of all parameters to be updated at time t
N : Number of output variables of the neural network identification model
$H(x_t)$: Hessian matrix
$A(x_t)$: Jacobian matrix
$e(x_t)$: Neural network error vector
μ : Damping parameter
N_1,N_2 : Range of the error prediction time domain
N_u : Control increment time domain range
y_r : Desired response output value of the controlled object system
y_m : Response output value of the neural network identification model
ρ : Contribution coefficient of the sum of squares of control increments to the performance index function
u' : Transitional control signal
u : Control variable
p_k : Descent direction
p_t : Neural network identification model input vector
t_0 : Start time of the tracking curve
t_1 : End time of the tracking curve
y_p : Output of the controlled object system

REFERENCES

[1] Cheng, Z.; Lu, Z.; Qian, J. A new non-geometric transmission parameter optimization design method for HMCVT based on improved GA and maximum transmission efficiency, *Computers and Electronics in Agriculture* 2019, 167. https://doi.org/10.1016/j.compag.2019.105034

[2] Wang, J.; Xia, C.; Fan, X.; Cai, J. Research on transmission characteristics of hydromechanical continuously variable transmission of tractor, *Mathematical Problems in Engineering* 2020, 2020 (1). https://doi.org/10.1155/2020/6978329

[3] Cheng, Z.; Lu, Z. System response modeling of HMCVT for tractors and the comparative research on system identification methods, *Computers and Electronics in Agriculture* 2022, 202. https://doi.org/10.1016/j.compag.2022.107386

[4] Wang, J.; Xia, C.; Fan, X.; Cai, J. Research on the influence of tractor parameters on shift quality, based on uniform design, *Applied Sciences-Basel* 2022, 12 (10), 4895. https://doi.org/10.3390/app12104895

[5] Yang, S.; Bao, Y.; Tang, X.; Jiao, X.; Yang, D.; Wang, Q. Integrated control of hydromechanical variable transmissions, *Mathematical Problems in Engineering* 2015, 2015 (1). https://doi.org/10.1155/2015/290659

[6] Hu, H.; Zhang, Q.; Fang, J.; Wang, T.; Wei, J. Practical adaptive robust tracking control of the dual-valve parallel electro-hydraulic servo system with reduced-order model, *Transactions of the Institute of Measurement and Control* 2024, 46 (3), 501-512. https://doi.org/10.1177/01423312231183200

[7] Zeng, X.; Liu, C.; Li, W.; Song, D.; Li, L.; Chen, C. Research on pump displacement control of hydraulic hybrid system, *Journal of Hunan University (Natural Sciences)* 2019, 46 (4), 25-33.

[8] Lin, S.; An, G.; Ji, Y.; Guo, Y. Nonlinear control of variable displacement mechanism for electro-hydraulic servo variable displacement pump, *Chinese Hydraulics and Pneumatics* 2020, 3, 107-112.

[9] Cao, F.; Li, H.; Yan, X.; Xu, L. Hydro-mechanical compound transmission constant rotational speed output control method under step input based on double feedforward and fuzzy PID, *Transactions of the CSAE* 2019, 35 (1), 72-82.

[10] Lu, Z.; Lu, ZX.; Cheng, Z. Research on tracking speed control of HMCVT stepless segment, *Mechanical Science and Technology for Aerospace Engineering* 2021, 40 (4), 518-526.

[11] Kong, X.; Song, Y.; Ai, C. Constant speed control method of variable speed input fixed displacement pump-constant speed output variable motor system, *Journal of Mechanical Engineering* 2016, 52 (8), 179-190. https://doi.org/10.3901/JME.2016.08.179

[12] Shen, W.; Cui, X. Modeling and simulation analysis of speed servo system with pump controlled hydraulic motor, *Hydraulics Pneumatics and Seals* 2019, 39 (1), 80-86.

[13] Bao, M.; Ni, X.; Zhao, X.; Han, S. Research on adaptive fuzzy PID joint simulation of HMCVT hydraulic system, *Machine Tool and Hydraulics* 2020, 48 (15), 177-183.

[14] Huang, X.; Lu, Z.; Chen, L.; An, Y. Research on fuzzy PID control of HMCVT pump-controlled-motor system, *Acta Agriculturae Universitatis Jiangxiensis* 2023, 45 (1), 189-201.

[15] Ülker, H. Design and application of an artificial neural network controller imitating a multiple model predictive controller for stroke control of hydrostatic transmission, *Machines* 2025, 13 (9), 778. https://doi.org/10.3390/machines13090778

[16] Gregov, G. Modeling and predictive analysis of the hydraulic GEROLER motor based on artificial neural network, *Engineering Review* 2022, 42 (2), 91-100. https://doi.org/10.30765/er.1813

[17] Xi, Y. *Predictive control*, 2nd Ed. National defense industry press, Beijing, China, 2013.

[18] Mao, H.; Tang, X.; Tang, H. Speed control of PMSM based on neural network model predictive control, *Transactions of the Institute of Measurement and Control* 2022, 44 (14), 2781-2794. https://doi.org/10.1177/01423312221086267

[19] Ding, H.; Zhao, J. Characteristic analysis of pump controlled motor speed servo in the hydraulic hoister, *International Journal of Modelling, Identification and Control* 2013, 19 (1), 64-74. https://doi.org/10.1504/IJMIC.2013.054038

[20] Zmak, I.; Filetin, T. Predicting thermal conductivity of steels using artificial neural networks, *Transactions of FAMENA* 2010, 34 (3), 11-20.

[21] Mirzaee, H. Long-term prediction of chaotic time series with multi-step prediction horizons by a neural network with Levenberg-Marquardt learning algorithm, *Chaos, Solitons & Fractals* 2009, 41 (4), 1975-1979. https://doi.org/10.1016/j.chaos.2008.08.016

[22] Bilski, J.; Smoląg, J.; Kowalczyk, B.; Grzanek, K.; Izonin, I. Fast computational approach to the Levenberg-Marquardt algorithm for training feedforward neural networks, *Journal of Artificial Intelligence and Soft Computing Research* 2023, 13 (2), 45-61. https://doi.org/10.2478/jaiscr-2023-0006

[23] Iskrenovic-Momcilovic, O. A discrete-time sliding mode controller for the fermentation process, *Transactions of FAMENA* 2021, 45 (2), 75-88. https://doi.org/10.21278/TOF.452022220

[24] Jian, N.L.; Zabiri, H.; Ramasamy, M. Control of the multi-timescale process using multiple timescale recurrent neural network-based model predictive control, *Industrial and Engineering Chemistry Research* 2023, 62 (15), 6176-6195. https://doi.org/10.1021/acs.iecr.2c04114

[25] Dennis Jr, J.E.; Schnabel, R.B. *Numerical methods for unconstrained optimization and nonlinear equations*. Science Press, Beijing, China, 2009.

[26] Ghafouri, M.; Daneshmand, S. Design and evaluation of an optimal fuzzy PID controller for an active vehicle suspension system, *Transactions of FAMENA* 2017, 41 (2), 29-44. https://doi.org/10.21278/TOF.41203

[27] Cai, J.; Jiang, H.; Wang, j. Implementation of the human-like lane changing driver model based on Bi-LSTM, *Discrete Dynamics in Nature and Society* 2022, 2022 (1). https://doi.org/10.1155/2022/9934292

[28] Arık, A.E.; Bilgiç, B. Fuzzy control of a landing gear system with oleo-pneumatic shock absorber to reduce aircraft vibrations by landing impacts, *Aircraft Engineering and Aerospace Technology* 2023, 95 (2), 284-291. https://doi.org/10.1108/AEAT-01-2022-0028

Submitted: 09.5.2025

Accepted: 21.01.2026

Junyan Wang
School of Transportation, Zhenjiang College, Zhenjiang China

Xin Fan
School of Automotive and Traffic Engineering, Jiangsu University, Zhenjiang China

Junyu Cai*
School of Automotive Engineering, Changzhou Institute of Technology, Changzhou China

*Corresponding author:
caijy@czust.edu.cn